

High-efficiency spin-decoupled modulation using chiral C_2 -symmetric meta-atomsHaohan Chen ¹, Jiepeng Wu,¹ Minglei He,¹ Hao Wang ¹, Xinen Wu,¹ Kezhou Fan,² Haiying Liu,¹ Qiang Li,¹ Kam Sing Wong,² and Lijun Wu ^{1,*}¹*Guangdong Basic Research Center of Excellence for Structure and Fundamental Interactions of Matter, Guangdong Provincial Key Laboratory of Nanophotonic Functional Materials and Devices, School of Information and Optoelectronic Science and Engineering, South China Normal University, Guangzhou 510006, China*²*Department of Physics and William Mong Institute of Nano Science and Technology, Hong Kong University of Science and Technology, Hong Kong 999077, China*

(Received 11 August 2023; accepted 5 December 2023; published 24 January 2024)

Orthogonal circularly polarized light is essential for multiplexing tunable metasurfaces. Mainstream spin-decoupled metasurfaces, consisting of numerous meta-atoms with mirror symmetry, rely on the cooperative modulation of the Pancharatnam-Berry (PB) phase and the propagation phase. This paper demonstrates spin-decoupled functionality through the synergistic utilization of planar chiral meta-atom phase response and the PB phase. Based on the Jones calculus, it has been found that meta-atoms with chiral C_2 symmetry possess a larger geometric parameter range with high cross-polarization ratio compared to those with mirror symmetry or higher symmetries at the same aspect ratio. This characteristic is advantageous in terms of enabling high-efficiency manipulation and enhancing the signal-to-noise ratio. As an example, 10 kinds of C_2 -symmetric chiral meta-atoms with a H-like shape are selected by the self-adaptive genetic algorithm to attain a full 2π phase span with an interval of $\pi/5$. To mitigate the additional propagation phase change of the guided modes originating from the arrangement alternation upon the rotation of the meta-atoms, the enantiomer of chiral meta-atoms and its PB phase delay are adopted to minimize the difference between the actual and desired target phases. A polarization-insensitive metalens and a chiral virtual-moving metalens array are designed to demonstrate the spin-decoupled function with both high efficiency and signal-to-noise ratio. The work in this paper may trigger more exciting and interesting spin-decoupled multiplexing metasurfaces and broaden the prospect of chiroptical applications.

DOI: [10.1103/PhysRevA.109.013517](https://doi.org/10.1103/PhysRevA.109.013517)**I. INTRODUCTION**

Metasurfaces [1], consisting of planar periodic subwavelength artificial meta-atoms, have attracted unprecedented attention because of the flexibility to manipulate light. Unlike conventional optical devices that rely on phase accumulation, metasurfaces provide a novel platform for electromagnetic wave manipulation through the generalized Snell's law [2,3]. Dozens of fascinating functionalities have been proposed, such as metalens [4,5], holograms [6,7], and vortex beam generators [8,9], to name but a few. In recent years versatile multiplexing tunable metasurfaces have been demonstrated by active [10–13] or passive [6,7,14–18] switching. Comparing with active switching, passive switching metasurfaces are easier to fabricate and exhibit more stable performances. Among the various passive switching methods, polarization serves as a key parameter for convenient and robust modulation through the use of a polarizer.

Typically, polarization-based multiplexing metasurfaces, comprising anisotropic nano-antennas, can be independently modulated through orthogonal polarization channels (e.g., orthogonal linear [14], circular [6,7], or elliptical [7] polarization). Among these channels, the independent modulation

of orthogonal circular polarization holds great importance in various applications, including dual-channel holograms [6,7], pancake metalenses [19], vector visual cryptography [20], and others. Considerable efforts have been demonstrated to realize the spin-decoupled function, employing various approaches such as the combination of the propagation phase and Pancharatnam-Berry (PB) phase [7,20], area division based on the PB phase [21,22], planar chiral meta-atoms [6,23], the combination of the Aharonov-Anandan phase and PB phase [24], and other methods [25,26]. For the aforementioned modulation methods, the presence of the nonmodulated polarization component noticeably contributes to the main background noise and thereby deteriorates the signal-to-noise ratio.

Increasing the number of meta-atoms with a high cross-polarization ratio (CPR) [21] is crucial for improving the phase modulation efficiency and signal-to-noise ratio of metasurfaces. For dielectric metasurfaces, it is evident that utilizing materials with a high refractive index or increasing the aspect ratio of meta-atoms can expand the pool of meta-atoms with both high transmission and high CPR [4,27]. Nevertheless, the fabrication of meta-atoms with large aspect ratios poses a substantial challenge. Another method involves broadening the diversity of the basic shape of meta-atoms in searching for more appropriate shapes [27,28], which in turn increases the computational resource requirements.

*Corresponding author: ljwu@scnu.edu.cn

Consequently, there is significant demand for identifying design restrictions on the basic shape to increase the quantity of high-efficiency meta-atoms at a specific aspect ratio, which can shorten the optimization process. On the other hand, structural symmetry plays a fundamental role in determining the physical properties of meta-atoms [29]. For example, various symmetrical meta-atoms result in different PB phase delays, in both linear [30] and nonlinear [31] regions. The symmetry of meta-atoms could be a vital parameter that impacts the abundance of meta-atoms with a high CPR.

In this work, based on the Jones calculation, we explore the influence of the structural symmetry on the geometric parameter range of the meta-atoms with high CPR. For a given basic shape, our findings indicate that planar meta-atoms with chiral C_1 and C_2 symmetries exhibit a greater number of instances with high CPR compared to those with mirror and higher symmetries, whereby phase modulation efficiency and signal-to-noise ratio can be increased. Compared to C_1 symmetry, C_2 symmetry requires fewer computing resources due to the reduced number of variables associated with a fixed basic shape. As an example, this paper utilizes a self-adaptive genetic algorithm to carefully select 10 types of C_2 -symmetric chiral meta-atoms with a H-like shape. By employing PB phase modulation and optimizing through its enantiomer, these 10 kinds of chiral meta-atoms enable the effective implementation of the spin-decoupled modulation function by covering the entire 2π phase range with an interval of $\pi/5$ for the orthogonal circular polarization (CP). The design strategy employed in this spin-decoupled phase library effectively reduces the number of required meta-atoms, thereby minimizing the design complexity and reducing the processing time. As any polarized light can be decomposed into two orthogonal CPs, a polarization-insensitive metalens is designed using the phase library, with both types of CP maintaining the same phase response. In addition, by manipulating the phase delay of these orthogonal CPs, a chiral virtual-moving metalens array is constructed, which can improve the spatial resolution of light-field imaging [14,32]. Our work will enrich the domain of high efficiency spin-decoupled modulation metasurfaces and may prompt more wonderful chiroptical applications.

II. CPR OF DIFFERENT SYMMETRIC META-ATOMS

As illustrated in Fig. 5(a) below, anisotropic nano-antennas with mirror symmetry (e.g., nanorods) exhibit a limitation wherein only the induced current flowing in the same direction can be excited when a linearly polarized electric field impinges along one of their optical axes. As a result, they are unable to generate disparate phase shifts for orthogonal CP light. In contrast, in nano-antennas with broken mirror symmetry, as depicted in Fig. 5(b), the induced current flow in the orthogonal direction can be excited. This capability potentially results in distinct phase shifts for different CP light.

In the case of subwavelength anisotropic nano-antennas, the excited electric field is commonly modeled as an electric dipole, where the dipole moment is assumed to be parallel in the x - y plane. When CP light is incident, the perpendicular radiation electric field E_t can be derived as (see Appendix A for more details)

$$\vec{E}_t = \begin{cases} A_0(p_{LL}\vec{s}_L + p_{RL}\vec{s}_R) \\ = A_0(A_1e^{j\varphi_1}\vec{s}_L + A_2e^{-j\varphi_2}\vec{s}_R), & I_L \\ A_0(p_{LR}\vec{s}_L + p_{RR}\vec{s}_R) \\ = A_0(A_2e^{j\varphi_2}\vec{s}_L + A_1e^{-j\varphi_1}\vec{s}_R), & I_R \end{cases}, \quad (1)$$

$$A_0 = \frac{-\omega^2}{4\pi\epsilon_0c^2R_0}e^{jkR_0}$$

$$A_1 = \frac{\epsilon_0}{2}\sqrt{(\chi_{xx} + \chi_{yy})^2 + (\chi_{xy} - \chi_{yx})^2}$$

$$A_2 = \frac{\epsilon_0}{2}\sqrt{(\chi_{xx} - \chi_{yy})^2 + (\chi_{xy} + \chi_{yx})^2}$$

$$\varphi_1 = \arctan \frac{\chi_{xy} - \chi_{yx}}{\chi_{xx} + \chi_{yy}}$$

$$\varphi_2 = -\arctan \frac{\chi_{xy} + \chi_{yx}}{\chi_{xx} - \chi_{yy}}, \quad (2)$$

where p_{LL} , p_{LR} , p_{RL} , and p_{RR} are the electric dipole moments in circular base. The subscript of R or L refers to RCP or LCP. I_L and I_R represent RCP and LCP incidences. χ_{xx} , χ_{xy} , χ_{yx} , and χ_{yy} are the electric polarizability tensors in linear orthogonal base. \vec{s}_L and \vec{s}_R are the unit vectors in the circular base of LCP and RCP, respectively. R_0 is the distance between the observation point and the electric dipole. c and ϵ_0 are the velocity of light and the permittivity in vacuum.

Equation (1) shows that the amplitude of the transmitted electric field, which exhibits the same or opposite chirality to the incident light, is given by A_0A_1 or A_0A_2 . For a planar chiral meta-atom without mirror symmetry, the cross-component polarizability tensor is $\chi_{xy} \neq 0$ and $\chi_{yx} \neq 0$. Under LCP (RCP) illumination, the transmission of light with the same or opposite handedness compensates the phase of $\varphi_1(-\varphi_1)$ or $-\varphi_2(\varphi_2)$, showcasing the spin-decoupled function of planar chiral meta-atoms in a manner reminiscent of PB phase modulation.

CPR is defined as [21]

$$\text{CPR}_{RL(LR)} = \frac{T_{RL(LR)}}{T_{RL(LR)} + T_{LL(RR)}}, \quad (3)$$

where T_{RL} , T_{LR} , T_{RR} , and T_{LL} represent the transmittance for different combinations of incidents (the second subscript letter) and transmitted (the first subscript letter) polarizations. For example, T_{RL} represents the transmittance of RCP for LCP incidents. All the same subscripts in the paper represent the same meaning unless otherwise specified.

Combining Eqs. (1)–(3), CPR can be deduced to be

$$\text{CPR} = \frac{A_2^2}{A_1^2 + A_2^2} = \frac{(\chi_{xx} - \chi_{yy})^2 + (\chi_{xy} + \chi_{yx})^2}{(\chi_{xx} + \chi_{yy})^2 + (\chi_{xy} - \chi_{yx})^2 + (\chi_{xx} - \chi_{yy})^2 + (\chi_{xy} + \chi_{yx})^2}. \quad (4)$$

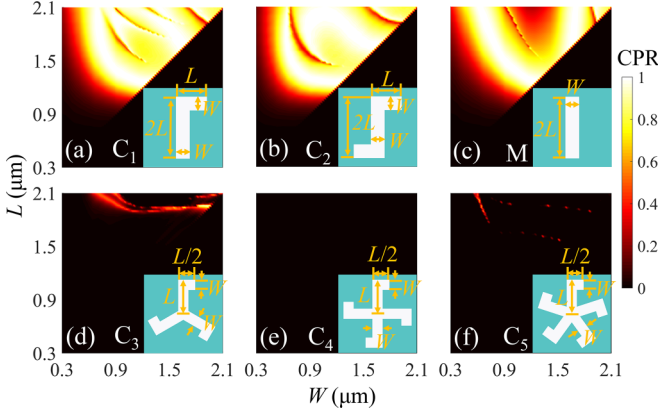


FIG. 1. CPR map as a function of the geometric parameters L and W ($L > W$) for different symmetric meta-atoms at a wavelength of $10.6 \mu\text{m}$. Inset: Schematic diagram illustrates meta-atoms with various symmetries, having a height of $6.8 \mu\text{m}$ and a period of $4.6 \mu\text{m}$

Various meta-atoms possess distinctive polarizability tensors. Constrained by structural symmetry, these polarizability tensors are confined within specific ranges, enabling the establishment of a connection between CPR and symmetry using Eq. (4). For mirror symmetric meta-atoms, the electric polarizability tensor satisfies $\chi_{xy} = \chi_{yx} = 0$, $\chi_{xx} \neq \chi_{yy} \neq 0$; C_1 -symmetric meta-atoms without mirror symmetry satisfy $\chi_{xx} \neq \chi_{yy} \neq \chi_{xy} \neq \chi_{yx} \neq 0$; C_2 -symmetric meta-atoms without mirror symmetry satisfy $\chi_{xy} = \chi_{yx} \neq 0$, $\chi_{xx} \neq \chi_{yy} \neq 0$; and C_n -symmetric ($n > 2$) meta-atoms satisfy $\chi_{xy} = -\chi_{yx}$, $\chi_{xx} = \chi_{yy}$ [29]. Based on Eq. (4), the value of CPR with different symmetries can be described as follows (see Appendix B for more details):

$$\text{CPR}_{C_1}, \text{CPR}_{C_2} > \text{CPR}_M > \text{CPR}_{C_n} \quad (n > 2). \quad (5)$$

In meta-atom design, the polarization conversion efficiency (PCE) is a more commonly used parameter compared to the CPR, as PCE encompasses information about transmittance. The PCE of meta-atoms can be obtained by calculating the product of CPR and the transmittance, with the latter being determined by the structure's shape and material properties. Maximizing CPR is therefore crucial to improve PCE of the structure. Indeed, it is essential to acknowledge that Eq. (5) is valid only under the assumption that the polarizability tensors of each symmetric structure are identical. However, satisfying the assumption is often challenging. In other words, Eq. (5) implies that within a given basic shape and parameter space, the number of meta-atoms with chiral C_1 and C_2 symmetry exhibiting high CPR is larger compared to those with mirror or other higher symmetric counterparts. Due to the substrate being a single layer with a thickness significantly larger than the wavelength, and considering the low refractive index of the substrate along with the high refractive index of the meta-atoms, the out-of-plane symmetry-breaking induced by a substrate can be neglected in our conclusion outlined in Eq. (5). As an example, Fig. 1 illustrates the CPR of various meta-atoms with different symmetries. Further information regarding the PCE and transmittance of these meta-atoms can be found in Figs. 6 and 7 below, respectively. For the sake of a straightforward comparison, the

parameters have been simplified to L and W ($L > W$). As shown, the transmittance of various symmetric meta-atoms shows similarities (Fig. 7). However, it is obvious that C_1 - and C_2 -symmetric chiral meta-atoms have a notably larger region with high CPR compared to meta-atoms with mirror and higher symmetries (Fig. 1). Consequently, C_1 - and C_2 -symmetric chiral meta-atoms demonstrate significantly higher PCE within this extended region compared to those with mirror and higher symmetries (Fig. 6). Since the CPR derived in Eq. (4) is based on the dipole approximation, and the dipole is the dominant radiation mode for the majority of basic shapes, the conclusion in Eq. (5) is applicable in most cases.

Based on the reasons given above and the fact that an unrestricted meta-atom with C_1 symmetry has too many geometric parameters to define, we adopt the constraint of chiral C_2 symmetry in the design of the meta-atoms for this paper. The transmission electric field \vec{E}_t^f of the chiral C_2 -symmetric meta-atoms under forward illumination along the z direction can be expressed as (see Appendix C for more details)

$$\vec{E}_t^f = \begin{cases} A_0(p_{LL}\vec{s}_L + p_{RL}\vec{s}_R) \\ = A_0(A_1\vec{s}_L + A_2e^{-j\varphi_2}\vec{s}_R), I_L \\ A_0(p_{LR}\vec{s}_L + p_{RR}\vec{s}_R) \\ = A_0(A_2e^{j\varphi_2}\vec{s}_L + A_1\vec{s}_R), I_R \end{cases}, \quad (6)$$

$$A_1 = \frac{\epsilon_0}{2} \sqrt{(\chi_{xx} + \chi_{yy})^2}$$

$$A_2 = \frac{\epsilon_0}{2} \sqrt{(\chi_{xx} - \chi_{yy})^2 + (2\chi_{xy})^2}$$

$$\varphi_1 = 0$$

$$\varphi_2 = -\arctan \frac{2\chi_{xy}}{\chi_{xx} - \chi_{yy}}. \quad (7)$$

III. DESIGN OF META-ATOMS WITH H-LIKE SHAPE

Under CP light illumination, the PB phase ϕ_{PB} (or so-called geometric phase) for an anisotropic meta-atom rotated around its geometric center by an angle θ can be expressed as [33]

$$\phi_{\text{PB}} = \arg \left[\cos^2 \left(\frac{\delta}{2} \right) + \sin^2 \left(\frac{\delta}{2} \right) e^{-2j\sigma\theta} \right], \quad (8)$$

where δ is the retardation between the long and short axes, which can be calculated as the phase difference between x - and y -polarized electric field incidence, that is, $\delta = \arg(E_{yt}) - \arg(E_{xt})$. σ equal to -1 or 1 for RCP or LCP illumination. When the anisotropic meta-atom meets the condition of a half-wave plate ($\delta = \pi$), the ideal PB phase is

$$\phi_{\text{PB}} = -2\sigma\theta. \quad (9)$$

By combining the PB phase modulation and the phase delay of the planar chiral meta-atom, the Jones matrix in circular basis can be expressed as

$$J(\theta) = \begin{bmatrix} t_{RR}e^{j\phi_{\chi RR}} & t_{RL}e^{j(\phi_{\chi RL} + \phi_{\text{PB}})} \\ t_{LR}e^{j(\phi_{\chi LR} + \phi_{\text{PB}})} & t_{LL}e^{j\phi_{\chi LL}} \end{bmatrix}, \quad (10)$$

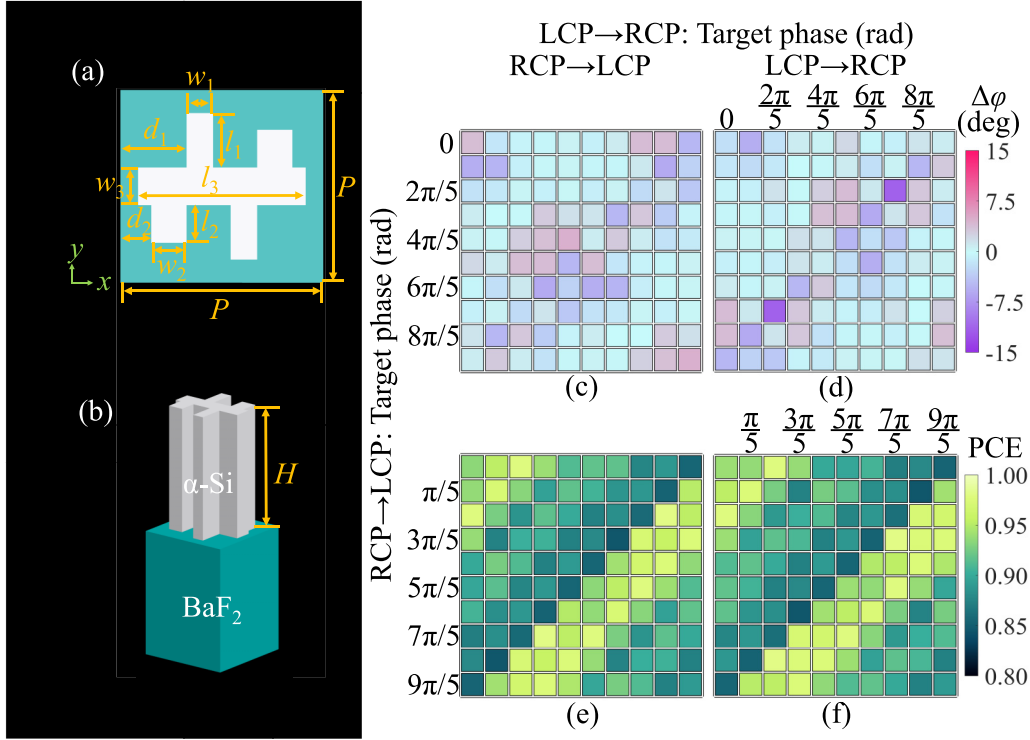


FIG. 2. (a), (b) Schematic top and side views of the H-like-shaped meta-atom. Geometric parameters are marked by yellow arrows. The meta-atom height $H = 6.8 \mu\text{m}$, period $P = 4.6 \mu\text{m}$. (c), (d) Phase difference ($\Delta\phi$) between reality and target in the phase library (optimized through the combination of meta-atoms and their enantiomers). (e), (f) Map of the polarization conversion efficiency (PCE) for the chosen meta-atoms. Color bar is normalized by Fig. 11.

where t_{RR} , t_{RL} , t_{LR} , and t_{LL} are the transmission amplitude, and $\phi_{\chi^{RR}}$, $\phi_{\chi^{RL}}$, $\phi_{\chi^{LR}}$, and $\phi_{\chi^{LL}}$ are the phase response of the chiral meta-atom, respectively. It should be known that the phase response of the chiral meta-atom can be expressed as the combination of the phase delay from the guided mode propagation ϕ_P and the additional phase delay caused by the electric dipole radiation in the chiral meta-atom $\pm\phi_{1(2)}$ in Eq. (2), that is,

$$\begin{aligned}\phi_{\chi^{RR}} &= \phi_P - \phi_1 \\ \phi_{\chi^{RL}} &= \phi_P - \phi_2 \\ \phi_{\chi^{LR}} &= \phi_P + \phi_2 \\ \phi_{\chi^{LL}} &= \phi_P + \phi_1.\end{aligned}\quad (11)$$

From Eq. (11), it can be seen that the chiral meta-atom is spin-decoupled when either ϕ_1 or ϕ_2 is nonzero. The independent total phase delay can be described by

$$\begin{aligned}\phi_{RR} &= \phi_{\chi^{RR}} = \phi_P - \phi_1 \\ \phi_{RL} &= \phi_{\chi^{RL}} + \phi_{PB} = \phi_P - \phi_2 + \phi_{PB} \\ \phi_{LR} &= \phi_{\chi^{LR}} + \phi_{PB} = \phi_P + \phi_2 + \phi_{PB} \\ \phi_{LL} &= \phi_{\chi^{LL}} = \phi_P + \phi_1.\end{aligned}\quad (12)$$

Equation (12) shows that the PB phase is applicable only to the cross-polarization. Additionally, as indicated in Eq. (7), for chiral C_2 -symmetric meta-atoms, ϕ_1 is zero. This leads to the copolarization without spin-decoupled functionality. Therefore, the cross-polarization component plays a central role in independently modulating spin light.

In order to improve the modulation efficiency and the signal-to-noise ratio, it is significant to minimize the circular dichroism [21,25] of the chiral meta-atoms and promote the cross-polarization ratio.

As discussed in Sec. II and illustrated in Fig. 5(b), adding small rectangles to both sides of a nanofin to break the mirror symmetry can excite induced current flow in the orthogonal direction and generate distinct phase shifts for different CP light. To enhance this induced current flow and increase the number of optimizable parameters, we introduce two small rectangles on either side of a nanofin, forming a H-like shaped meta-atom with 8 variable geometric parameters, as depicted in Fig. 2(a). The basic shape adheres to the chiral C_2 symmetry. As is well-known, longer operating wavelengths correspond to larger meta-atom sizes, which are generally easier to fabricate. Here $10.6 \mu\text{m}$ corresponds to the output wavelength of CO₂ lasers [34] and serves as the effective wavelength for SF₆ gas detection [35]. Therefore, we set the working wavelength to be $10.6 \mu\text{m}$ in this paper. Please note that the design method presented here can be easily extended to other wavelengths, ensuring its applicability and versatility. In the numerical simulations, the meta-atoms are chosen to be amorphous Si nano-antennas ($n_{\text{Si}} = 3.7400$) [36] on a BaF₂ substrate ($n_{\text{BaF}_2} = 1.4069$) [37] with height $H = 6.8 \mu\text{m}$ and period $P = 4.6 \mu\text{m}$, which can be obtained by a state-of-the-art standard nanofabrication technology [34]. The finite-difference time-domain (FDTD) method (FDTD Solutions, Lumerical, Canada) is used for numerical calculations here (see Appendix D for more details). To efficiently explore the vast design space and handle numerous variables of the meta-

TABLE I. Parameters of 10 optimized meta-atoms with H-like shape.

No.	W_1 (μm)	W_2 (μm)	W_3 (μm)	L_1 (μm)	L_2 (μm)	L_3 (μm)	d_1 (μm)	d_2 (μm)
1	0.758	0.461	0.680	0.427	0.291	3.444	1.768	0.628
2	0.411	0.469	0.886	0.713	0.460	2.839	1.405	1.161
3	0.513	0.439	1.068	0.311	0.574	3.408	0.810	1.577
4	0.491	0.549	1.351	0.306	0.383	3.037	1.090	0.870
5	0.966	0.470	1.633	0.010	0.119	3.239	0.892	0.860
6	1.247	0.625	0.585	0.501	0.042	3.562	1.295	0.614
7	0.891	0.433	1.113	0.398	0.310	2.482	1.275	1.132
8	0.428	0.674	1.269	0.887	0.059	2.877	1.241	1.410
9	1.059	0.564	0.991	0.639	0.385	3.636	1.054	1.075
10	1.303	0.588	1.259	0.370	0.191	3.621	1.198	0.620

atom, an optimization algorithm [38,39] is utilized to expedite the structure screening process. To avoid converging to local optimal solutions, an adaptive genetic algorithm is implemented in the optimization process (see Appendix E for more details). Figure 10 in Appendix H illustrates the schematic diagram of 10 optimized meta-atoms, and Table I provides the respective parameters for each of them. Table II presents the specific phase, PCE, CPR, and transmission values.

By combining 10 optimized meta-atoms and their PB phase delay, a spin-decoupled phase library is built spanning the full 2π range with an interval of $\pi/5$. Figures 11(a) and 11(b) in Appendix H illustrate the presence of phase difference between the reality and the target in the phase library. We attribute these deviations to two factors. The first factor arises from the PB phase delay offset caused by the mismatch of retardation. According to Eq. (8), when the retardation of the meta-atom does not precisely satisfy the condition of $\delta = \pi$, there will be a PB phase delay offset compared to the ideal ϕ_{PB} obtained in Eq. (9) [33]. Figure 9(a) displays the actual retardations δ of the optimized meta-atoms, revealing that they are not exactly equal to π . Consequently, certain offsets exist. Figures 9(b) and 9(c) depict the offset when $\delta = 0.8\pi$ as an example. The second factor is related to the variations in the propagation phase delay ϕ_P of the guide mode, as given in Eq. (12). When the meta-atom is rotated, the relative position between adjacent meta-atoms changes [Fig. 9(d)], influencing the propagation phase delay ϕ_P .

Interestingly, the mirror symmetry operation on the C_2 -symmetric chiral meta-atoms yields a corresponding opposite phase response. Specifically, if the relation before the operation is $\varphi_{RL} = \varphi_a$ and $\varphi_{LR} = \varphi_b$, then it becomes $\varphi_{RL} = \varphi_b$ and $\varphi_{LR} = \varphi_a$ after the operation (see Appendix C for more details). Based on this symmetry characteristic, the enantiomer of the 10 optimized meta-atoms can also fulfill the requirements of the phase delay library, as shown in Figs. 11(e) and 11(f). Through meticulous comparison of the phase delay between the optimized meta-atoms and their enantiomers, we select those exhibiting minimal deviation from the target phase delay and put them into the phase library. Figures 2(c) and 2(d) display the phase difference of the optimized phase library. Obviously, the shown deviation is smaller than that either from the optimized meta-atoms [Figs. 11(a) and 11(b)] or their enantiomers [Figs. 11(e) and 11(f)]. Notably, the PCEs depicted in Figs. 2(e) and 2(f) are larger than 85% in the whole phase library, indicating high efficiency of the meta-atoms within the library.

IV. POLARIZATION-INSENSITIVE METALENS

To demonstrate the high modulation efficiency and signal-to-noise ratio of the chiral C_2 -symmetric meta-atoms with H-like shape, we utilize the phase library built in Sec. III to construct two polarization-insensitive metalenses with numerical aperture (NA) values of 0.80 and 0.40. As commonly known, any polarization can be decomposed into a pair of orthogonal polarization (e.g., x and y polarization or RCP and LCP). When the phase responses of RCP and LCP light are identical, it guarantees polarization-insensitive characters. As seen in Table II, the first through fifth H-like-shaped meta-atoms show the same phase response for RCP and LCP incidence. Thus, they are selected to construct the metalens as the schematic diagram of Fig. 3(a).

For RCP or LCP illumination, the phase at position (x, y) in space should satisfy the spherical focusing equation [4,5]:

$$\varphi_{LR/RL}(x, y, \lambda) = -\frac{2\pi}{\lambda}(\sqrt{x^2 + y^2 + f^2} - f), \quad (13)$$

where λ is the design wavelength and f is the focal length. Both a high NA metalens (radius $R = 161 \mu\text{m}$, focus length $f = 120 \mu\text{m}$, NA = 0.80) and a low NA metalens (radius $R = 161 \mu\text{m}$, focus length $f = 370 \mu\text{m}$, NA = 0.40) are constructed in this section. Figures 3(b) and 3(c) show the

TABLE II. Phase, polarization conversion efficiency (PCE), cross-polarization ratio (CPR), and transmission of 10 optimized meta-atoms.

No.		1	2	3	4	5	6	7	8	9	10
	Target phase ($^\circ$)	0	36	72	108	144	0	36	72	108	144
RCP	Actual phase ($^\circ$)	3.73	30.73	72.20	110.92	148.68	352.65	32.81	74.59	109.57	144.74
↓	PCE (%)	93.42	97.20	88.50	90.52	88.97	93.08	92.87	92.29	87.27	85.57
LCP	CPR (%)	99.84	98.79	92.68	99.02	99.64	99.80	97.90	99.33	97.12	98.33
	Transmission (%)	93.57	98.40	95.49	91.42	89.29	93.26	94.86	92.91	89.85	87.02
	Target phase ($^\circ$)	0	36	72	108	144	36	72	108	144	180
LCP	Actual phase ($^\circ$)	357.85	33.66	73.39	107.76	145.24	32.66	70.73	110.02	147.62	174.94
↓	PCE (%)	94.02	97.52	88.93	90.98	89.00	95.06	94.12	92.16	87.26	85.64
RCP	CPR (%)	99.85	98.75	92.92	99.07	99.64	99.82	97.78	99.30	97.08	98.37
	Transmission (%)	94.16	98.76	95.71	91.84	89.33	95.22	96.26	92.81	89.89	87.06

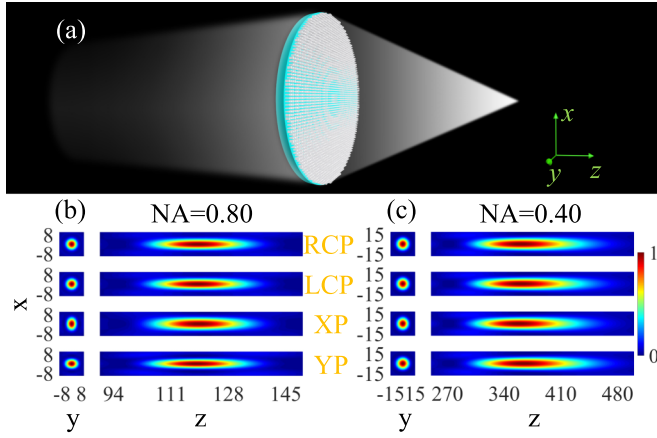


FIG. 3. (a) Schematic diagram illustrates a polarization-insensitive metalens with a radius of $161 \mu\text{m}$. (b), (c) Corresponding intensity profiles in the x - y and x - z plane with a focal length $f = 120 \mu\text{m}/370 \mu\text{m}$ for different polarization illuminations, with length units in microns. XP: x polarization; YP: y polarization.

far-field intensity profiles of the two metalenses, and Table III provides the specific information regarding the actual focus length, full width at half maximum (FWHM) and focusing efficiency. The actual focus length difference between two polarizations is observed to be less than 1.7% ($\Delta f/f$), indicating polarization-insensitive characteristics. Furthermore, FWHM approaches the diffraction limit ($\lambda/2\text{NA}$, $6.63 \mu\text{m}$ for $\text{NA} = 0.80$ and $13.25 \mu\text{m}$ for $\text{NA} = 0.40$), and the focusing efficiency reaches 76%, demonstrating high-quality focusing performance. Table IV presents a comparison of the focusing efficiency between this paper and those previously reported monochromatic polarization-insensitive metalenses operating in the long-wave infrared band. The results demonstrate highly competitive performance in terms of focusing efficiency. Notably, our metalens achieves diffraction-limited focusing with high focusing efficiency, without the need for a significantly increased aspect ratio of meta-atoms. Moreover, the metalens maintains its competitive focusing efficiency even when increasing the NA from 0.40 to 0.80.

As observed from Figs. 3(b) and 3(c) and Table III, the intensity profiles at the focus spot in the x - y plane exhibit asymmetry for both x and y polarizations. It is more obvious that $\text{NA} = 0.80$. It can be attributed to the radiation pattern of the electric dipole when excited by linear polarization, which deviates from a perfect spherical wave. The radiation power is highest in the direction perpendicular to the dipole moment, and it decreases as the radiation gets closer to the

TABLE IV. Comparison of focusing efficiency for long-wave infrared monochromatic polarization-insensitive metalenses. λ is the wavelength of incident light. P , H , and H/P are the period, height, and aspect ratio of meta-atoms, respectively. D , f , and NA are the diameter, focal length, and numerical aperture of metalenses, respectively. FE is focusing efficiency. DL and SL are double layer and single layer, respectively.

Year	2021	2021	2021	2022	2022	2019	2023	2023
λ (μm)	9	9	10.6	9.28	10	10.6	10.6	10.6
Structure	Si	Si	Si	Ge	Si	Si	α -Si	α -Si
Substrate	MgF_2	MgF_2	Si	BaF_2	Si	Si	BaF_2	BaF_2
P (μm)	3.6	3.6	3	4.84	3	5.5	4.6	4.6
H (μm)	4	4	25.8	1.425	8	6.8	6.8	6.8
H/P	1.11	1.11	8.6	0.29	2.67	1.24	1.48	1.48
D (μm)	100	197	90	300	60	100	322	322
f (μm)	88	85	50.3	240	300	100	370	120
NA	0.494	0.757	0.67	0.53	0.10	0.45	0.40	0.80
FE (%)	47.97	42.28	71	44.08	86	43	83	76
Layer	DL	DL	DL	DL	SL	SL	SL	SL
Ref.	[42]	[42]	[43]	[44]	[45]	[34]	This	This

dipole moment. Generally, the pattern of the dipole radiation in the linear base can be described as an ellipsoidal wave. The long axis of the ellipsoid is oriented perpendicular to the dipole moment, while the short axis is parallel to the dipole moment. The Huygens-Fresnel diffraction principle states that the intensity distribution at the focal point is formed through a coherent superposition of the subwavefronts emitted by each meta-atom on the metalens [40]. The linearly polarized incident light excites dipole radiation with the moment parallel to the metasurfaces and along with the polarization direction. Therefore, at the edge of the metalens, the angle between the dipole radiation and the moment direction becomes smaller at a higher NA. This leads to a more nonuniform intensity distribution pattern at the focal point. As a result, the focused spot of the metalens appears more elliptical for $\text{NA} = 0.80$ than 0.40 (see Appendix G for more details).

V. CHIRAL VIRTUAL-MOVING METALENS ARRAY

The virtual-moving metalens array has great potential in various applications, including high efficiency and high spatial resolution light field cameras [14,32], vector visual cryptography [20], multiphoton quantum sources [41], and so forth. In this section a chiral virtual-moving metalens array is designed to demonstrate the high-efficiency spin-decoupled multiplexing function of the H-like shaped meta-atoms. The

TABLE III. Detailed results for the polarization-insensitive metalens with radius $R = 161 \mu\text{m}$ and focal length $f = 120/370 \mu\text{m}$. FWHM: full width at half maximum.

NA	0.80				0.40			
	RCP	LCP	XP	YP	RCP	LCP	XP	YP
Incident polarization								
Focal length (μm)	118.67	118.67	119.10	118.46	359.51	359.51	356.70	362.64
x -FWHM (μm)	6.54	6.54	7.61	5.74	13.22	13.22	13.49	12.95
y -FWHM (μm)	6.54	6.54	5.74	7.61	13.22	13.22	12.69	13.76
Focusing efficiency (%)	76.12	76.64	77.54	78.13	82.97	82.74	82.15	83.94

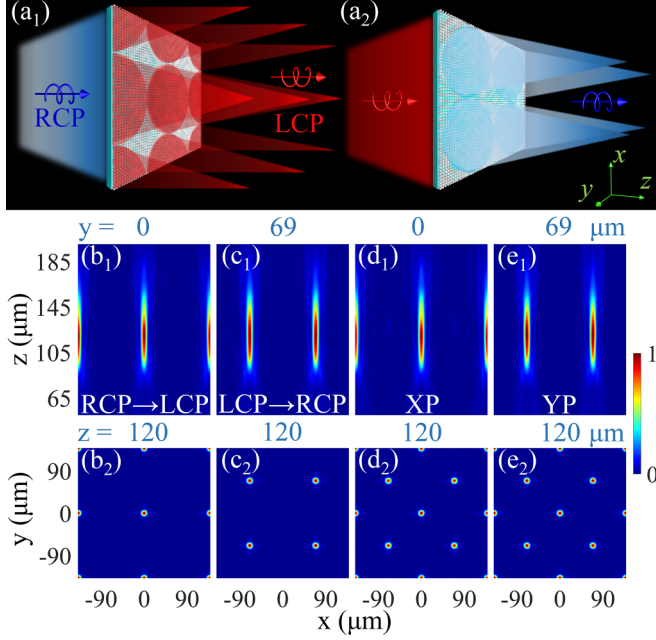


FIG. 4. (a) Schematic diagram of the 2×2 chiral virtual-moving metalens array. Side length and focus length of the metalens are $138 \mu\text{m}$ and $120 \mu\text{m}$, respectively. Blue and red arrows represent RCP and LCP light, respectively. (b–e) Corresponding intensity profiles in the x - y and x - z plane for different incident polarizations.

metalens array can efficiently focus different circularly polarized light into distinct spatial positions. The phase profiles responsible for the lateral separation of the focus spots are expressed as [14]

$$\begin{aligned} \varphi_{LR}(x, y, \lambda) &= -\frac{2\pi}{\lambda}(\sqrt{x^2 + y^2 + f^2} - f) \\ \varphi_{RL}(x, y, \lambda) &= -\frac{2\pi}{\lambda}(\sqrt{(x+R)^2 + (y+R)^2 + f^2} - f), \end{aligned} \quad (14)$$

where R is the radius of a single metalens. The above equation indicates that both RCP and LCP will converge at the same focal plane along the z axis, while they exhibit a displacement of radius R in the x - y plane. Figure 4(a) depicts the schematic diagram of the 2×2 chiral virtual-moving metalens array, where the side length and focal length are designed as $138 \mu\text{m}$ and $120 \mu\text{m}$, respectively. In Figs. 4(b)–4(e), the far-field intensity profiles are presented for different polarization illuminations, and the detailed focusing performance of the metalens array is provided in Table V. Notably, the focusing efficiency for both RCP and LCP reach 84%, with the FWHM of the focus spot closely approaching the diffraction limit ($8.41 \mu\text{m}$ for $\text{NA} = 0.63$).

VI. CONCLUSION

The design in this paper incorporates chiral meta-atoms and their PB phase delay to achieve independent control over spin light. Based on the Jones calculus, our findings demonstrate that chiral C_2 -symmetric meta-atoms have a greater likelihood of achieving a high cross-polarization ratio. Em-

TABLE V. Detailed results of the chiral virtual-moving metalens array with side length $D = 138 \mu\text{m}$ and focal length $f = 120 \mu\text{m}$, yielding $\text{NA} = 0.63$. FP: focal point position; FL: focal length.

Polarization	RCP	LCP	XP	XP	YP	YP
FP (x, y) (μm)	(0,0)	(69,69)	(0,0)	(69,69)	(0,0)	(69,69)
FL (μm)	120.40	119.09	120.03	116.27	121.15	120.21
x -FWHM (μm)	9.33	9.33	9.33	9.67	9.33	9.33
y -FWHM (μm)	9.33	9.67	9.33	9.67	9.33	9.33
FE (%)	84.28	84.22	42.46	42.67	44.09	43.73

ploying an adaptive genetic algorithm, 10 chiral C_2 -symmetric meta-atoms with a H-like shape were designed, allowing for the coverage of a full 2π phase span with intervals of $\pi/5$ for both spin light components through their rotation. To minimize deviations from the target phase delays, the phase library is updated by integrating the enantiomer of optimized meta-atoms. Utilizing the phase library, we designed a polarization-insensitive metalens and a virtual-moving metalens array to demonstrate their spin-decoupled functionality and high efficiency modulation. Our work has the potential to inspire further advancements in the field of chiral optics and polarization multiplexing metasurfaces, opening up exciting opportunities for future applications.

ACKNOWLEDGMENTS

This work was funded by the National Natural Science Foundation of China (NSFC; Grant No. 12274148), the Natural Science Foundation of Guangdong Province (Grant No. 2021A1515010286), and the project ‘‘Lightweight Lens Designing’’ from Guangzhou Keii Electro Optics Technology Co., Ltd. K.S.W. acknowledges the funding support of the Research Grants Council of Hong Kong (Grant No. 16304722).

APPENDIX A: DERIVATION OF THE RADIATION ELECTRIC FIELD

The circularly polarized (CP) electric field $\vec{E}_{\sigma i}$ illuminating along the z axis (vertical x - y plane) can be expressed as

$$\vec{E}_{\sigma i} = \begin{bmatrix} E_{xi} \\ E_{yi} \end{bmatrix} e^{j(kz - \omega t)} = \frac{1}{\sqrt{2}} \begin{bmatrix} 1 \\ \sigma j \end{bmatrix} e^{j(kz - \omega t)}, \quad (\text{A1})$$

where $\sigma = +1$ and -1 represent left-circular polarization (LCP) and right-circular polarization (RCP), respectively. The components \vec{E}_{xi} and \vec{E}_{yi} correspond to the x and y components of the incident electric field. j denotes the imaginary symbol of the complex number, while k represents the wave vector in vacuum and ω signifies the frequency of light.

The electric field response of the meta-atom can be modeled as an electric dipole \vec{p} . Normally, a meta-atom can excite only an electric dipole, leading to the polarization vector $\vec{P} = N\vec{p}$, where $N = 1$. The electric dipole moment of an anisotropic meta-atom can be written as

$$\begin{aligned} \begin{bmatrix} P_x \\ P_y \end{bmatrix} &= \begin{bmatrix} P_x \\ P_y \end{bmatrix} = \epsilon_0 \begin{bmatrix} \chi_{xx} & \chi_{xy} \\ \chi_{yx} & \chi_{yy} \end{bmatrix} \begin{bmatrix} E_{xi} \\ E_{yi} \end{bmatrix} \\ &= \frac{\epsilon_0}{\sqrt{2}} \begin{bmatrix} \chi_{xx} & \chi_{xy} \\ \chi_{yx} & \chi_{yy} \end{bmatrix} \begin{bmatrix} 1 \\ \sigma j \end{bmatrix}, \end{aligned} \quad (\text{A2})$$

where $\vec{p} = p_x \vec{e}_x + p_y \vec{e}_y$ is the electric dipole moment and $\vec{P} = \vec{P}_x \vec{e}_x + \vec{P}_y \vec{e}_y$ is the polarization vector. \vec{e}_x and \vec{e}_y are the unit vectors along x and y direction, respectively. ϵ_0 represents the permittivity in vacuum. χ_{xx} , χ_{xy} , χ_{yx} , and χ_{yy} correspond to the respective components of the electric polarizability tensor.

Changing from the Cartesian base to the circular base, the new base follows [29]

$$\begin{bmatrix} \vec{s}_L \\ \vec{s}_R \end{bmatrix} = \frac{1}{\sqrt{2}} \begin{bmatrix} 1 & j \\ 1 & -j \end{bmatrix} \begin{bmatrix} \vec{e}_x \\ \vec{e}_y \end{bmatrix} = \frac{1}{\sqrt{2}} \begin{bmatrix} \vec{e}_x + j\vec{e}_y \\ \vec{e}_x - j\vec{e}_y \end{bmatrix}, \quad (\text{A3})$$

where \vec{s}_L and \vec{s}_R are the unit vectors of the LCP and RCP, respectively. The electric dipole moment can be transformed as $\vec{p} = p_L \vec{s}_L + p_R \vec{s}_R$ [6], that is,

$$\begin{bmatrix} p_L \\ p_R \end{bmatrix} = \epsilon_0 \begin{bmatrix} \chi_{LL} & \chi_{LR} \\ \chi_{RL} & \chi_{RR} \end{bmatrix} \begin{bmatrix} E_{+i} \\ E_{-i} \end{bmatrix}, \quad (\text{A4})$$

$$\begin{aligned} \chi_{LL} &= 0.5[\chi_{xx} + \chi_{yy} + j(\chi_{xy} - \chi_{yx})] \\ \chi_{LR} &= 0.5[\chi_{xx} - \chi_{yy} - j(\chi_{xy} + \chi_{yx})] \\ \chi_{RL} &= 0.5[\chi_{xx} - \chi_{yy} + j(\chi_{xy} + \chi_{yx})] \\ \chi_{RR} &= 0.5[\chi_{xx} + \chi_{yy} - j(\chi_{xy} - \chi_{yx})]. \end{aligned} \quad (\text{A5})$$

The χ_{LL} , χ_{LR} , χ_{RL} , and χ_{RR} are the electric polarizability tensor in circular base. The formal equation can be further simplified as

$$\begin{aligned} \begin{bmatrix} p_L \\ p_R \end{bmatrix} &= \begin{bmatrix} A_1 e^{j\varphi_1} & A_2 e^{j\varphi_2} \\ A_2 e^{-j\varphi_2} & A_1 e^{-j\varphi_1} \end{bmatrix} \begin{bmatrix} E_{+i} \\ E_{-i} \end{bmatrix} \\ &= \begin{bmatrix} p_{LL} & p_{LR} \\ p_{RL} & p_{RR} \end{bmatrix} \begin{bmatrix} s_L \\ s_R \end{bmatrix}, \quad (\text{A6}) \\ A_1 &= \frac{\epsilon_0}{2} \sqrt{(\chi_{xx} + \chi_{yy})^2 + (\chi_{xy} - \chi_{yx})^2} \\ A_2 &= \frac{\epsilon_0}{2} \sqrt{(\chi_{xx} - \chi_{yy})^2 + (\chi_{xy} + \chi_{yx})^2} \\ \varphi_1 &= \arctan \frac{\chi_{xy} - \chi_{yx}}{\chi_{xx} + \chi_{yy}} \\ \varphi_2 &= -\arctan \frac{\chi_{xy} + \chi_{yx}}{\chi_{xx} - \chi_{yy}}. \end{aligned} \quad (\text{A7})$$

In the notations p_{LL} , p_{LR} , p_{RL} , and p_{RR} , the left-hand side subscripts indicate the chirality of the electric dipole radiation field, and the right-hand-side subscripts represent the chirality of the incident electric field. For instance, p_{LR} represents the electric dipole moment of the LCP component of the electric dipole radiation field when it is illuminated by RCP light. All

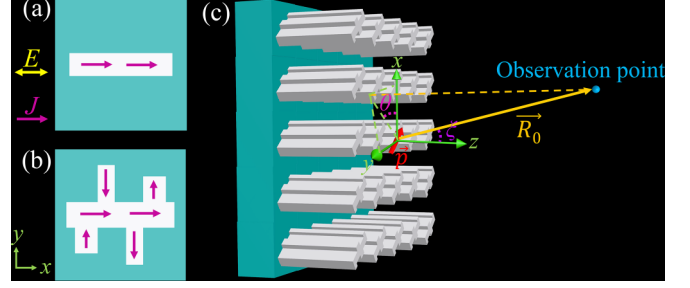


FIG. 5. (a), (b) Top view of the nanofin and the H-like-shaped meta-atom, with the purple arrows illustrating the current flow induced by the x -polarized electric field (yellow arrow). (c) Schematic diagram depicting the identification of coordinates.

the same subscripts in the paper represent the same meaning unless otherwise specified.

Therefore, the expression for the transmission electric field can be given as follows:

$$\vec{E}_t = \begin{cases} A_0 [p_{LL} \vec{s}_L + p_{RL} \vec{s}_R \\ - \frac{1}{\sqrt{2}} \sin \xi (p_{LL} + p_{RL}) \vec{e}_{R_0}], I_L \\ A_0 [p_{LR} \vec{s}_L + p_{RR} \vec{s}_R \\ - \frac{1}{\sqrt{2}} \sin \xi (p_{LR} + p_{RR}) \vec{e}_{R_0}], I_R \end{cases}, \quad (\text{A8})$$

where $A_0 = \frac{-\omega^2}{4\pi \epsilon_0 c^2 R_0} e^{jkR_0}$, R_0 is the distance between the observation point and the electric dipole, and c is the velocity of light in vacuum. I_L and I_R represent RCP and LCP incidences, respectively. The spatial unit vector \vec{e}_{R_0} is defined as $\vec{e}_{R_0} = \sin \xi \cos \theta \vec{e}_x + \sin \xi \sin \theta \vec{e}_y + \cos \xi \vec{e}_z$, where θ represents the angle between the projection of the line from the observation point to the origin of the coordinates in the x - y plane and the x axis, and ξ is the angle between the line from the observation point to the origin of the coordinates and z axis. A schematic diagram is available in Fig. 5(c).

When CP light is illuminating, the radiation electric field, which is perpendicular to the x - y plane (i.e., $\xi = 0$), can be simplified as

$$\vec{E}_t = \begin{cases} A_0 (p_{LL} \vec{s}_L + p_{RL} \vec{s}_R) \\ = A_0 (A_1 e^{j\varphi_1} \vec{s}_L + A_2 e^{-j\varphi_2} \vec{s}_R), I_L \\ A_0 (p_{LR} \vec{s}_L + p_{RR} \vec{s}_R) \\ = A_0 (A_2 e^{j\varphi_2} \vec{s}_L + A_1 e^{-j\varphi_1} \vec{s}_R), I_R \end{cases}. \quad (\text{A9})$$

APPENDIX B: DERIVATION OF CPR WITH DIFFERENT SYMMETRY

The cross-polarization ratio (CPR), as defined in Eqs. (3) and (4), can be expressed as follows:

$$\text{CPR} = \frac{A_2^2}{A_1^2 + A_2^2} = \frac{(\chi_{xx} - \chi_{yy})^2 + (\chi_{xy} + \chi_{yx})^2}{(\chi_{xx} + \chi_{yy})^2 + (\chi_{xy} - \chi_{yx})^2 + (\chi_{xx} - \chi_{yy})^2 + (\chi_{xy} + \chi_{yx})^2}. \quad (\text{B1})$$

Considering the forward illumination along the z direction, the Jones matrix of the electric polarizability tensor \hat{T}_{lin}^f can be expressed as [29]

$$\hat{T}_{lin}^f = \begin{bmatrix} \chi_{xx} & \chi_{xy} \\ \chi_{yx} & \chi_{yy} \end{bmatrix}, \quad (\text{B2})$$

where the superscript f represents forward propagation and the subscript lin represents the linear orthogonal base. For backward illumination along the $-z$ direction, the electric polarizability tensor \hat{T}_{lin}^b can be described as

$$\hat{T}_{lin}^b = \begin{bmatrix} \chi_{xx} & -\chi_{yx} \\ -\chi_{xy} & \chi_{yy} \end{bmatrix}, \quad (\text{B3})$$

where the superscript b represents backward propagation.

The transformation matrix D_β , which describes the rotation of the meta-atom by an angle β along the z axis, is given by

$$D_\beta = \begin{bmatrix} \cos(\beta) & \sin(\beta) \\ -\sin(\beta) & \cos(\beta) \end{bmatrix}. \quad (\text{B4})$$

The transformation matrices for mirror symmetry along the x - z plane M_x and y - z plane M_y can be expressed as

$$M_x = \begin{bmatrix} 1 & 0 \\ 0 & -1 \end{bmatrix}, \quad M_y = \begin{bmatrix} -1 & 0 \\ 0 & 1 \end{bmatrix}. \quad (\text{B5})$$

The electric polarizability tensor for the meta-atom with mirror symmetry along the x - z plane $\hat{T}_{M_x}^f$ or y - z plane $\hat{T}_{M_y}^f$ follows the relation as

$$M_x^{-1} \hat{T}_{M_x}^f M_x = \hat{T}_{M_x}^f, \quad M_y^{-1} \hat{T}_{M_y}^f M_y = \hat{T}_{M_y}^f. \quad (\text{B6})$$

$$\text{CPR}_{C_1} = \frac{A_2^2}{A_1^2 + A_2^2} = \frac{(\chi_{xx} - \chi_{yy})^2 + (\chi_{xy} + \chi_{yx})^2}{(\chi_{xx} + \chi_{yy})^2 + (\chi_{xy} - \chi_{yx})^2 + (\chi_{xx} - \chi_{yy})^2 + (\chi_{xy} + \chi_{yx})^2}. \quad (\text{B10})$$

The C_2 -symmetric meta-atom without mirror symmetry not only coincides with itself by rotating at a π angle along the z axis, but also coincides with the backward structure after mirror symmetry along the x - z or y - z plane. The electric polarizability tensor of the C_2 -symmetric chiral meta-atom satisfies the following relation:

$$D_\pi^{-1} \hat{T}_{C_2}^f D_\pi = \hat{T}_{C_2}^f, \quad M_x^{-1} \hat{T}_{C_2}^f M_x = \hat{T}_{C_2}^b. \quad (\text{B11})$$

By combining Eqs. (B2)–(B4) and (B11), it can be observed that $\chi_{xy} = \chi_{yx} \neq 0$ and $\chi_{xx} \neq \chi_{yy} \neq 0$. Therefore, for the C_2 -symmetric meta-atom without mirror symmetry, the electric polarizability tensor $\hat{T}_{C_2}^f$ can be expressed as

$$\hat{T}_{C_2}^f = \begin{bmatrix} \chi_{xx} & \chi_{xy} \\ \chi_{xy} & \chi_{yy} \end{bmatrix}. \quad (\text{B12})$$

By combining Eqs. (B1) and (B12), the CPR of the C_2 -symmetric chiral meta-atom can be described as

$$\begin{aligned} \text{CPR}_{C_2} &= \frac{A_2^2}{A_1^2 + A_2^2} \\ &= \frac{(\chi_{xx} - \chi_{yy})^2 + (2\chi_{xy})^2}{(\chi_{xx} + \chi_{yy})^2 + (\chi_{xx} - \chi_{yy})^2 + (2\chi_{xy})^2}. \end{aligned} \quad (\text{B13})$$

It is evident from Eqs. (B10) and (B13) that for C_1 -symmetric and C_2 -symmetric chiral meta-atoms, if $\chi_{xy} > \chi_{yx}$, then $\text{CPR}_{C_2} > \text{CPR}_{C_1}$, and vice versa.

The C_n -symmetric ($n > 2$) meta-atom without mirror symmetry coincides with itself by rotating at a $2\pi/n$ angle along

From Eq. (B6), it can be concluded that $\chi_{xy} = \chi_{yx} = 0$ and $\chi_{xx} \neq \chi_{yy} \neq 0$. Therefore, for the meta-atom with mirror symmetry, the electric polarizability tensor \hat{T}_M^f can be expressed as

$$\hat{T}_M^f = \hat{T}_{M_x}^f = \hat{T}_{M_y}^f = \begin{bmatrix} \chi_{xx} & 0 \\ 0 & \chi_{yy} \end{bmatrix}. \quad (\text{B7})$$

The electric polarizability tensor of the meta-atom with mirror symmetry at a certain angle along the x - z plane can be transformed to the form described in Eq. (B7) using Eq. (B4) and (B5). By combining Eq. (B1) and (B7), the CPR of the mirror symmetric meta-atom can be described as

$$\text{CPR}_M = \frac{A_2^2}{A_1^2 + A_2^2} = \frac{(\chi_{xx} - \chi_{yy})^2}{(\chi_{xx} + \chi_{yy})^2 + (\chi_{xx} - \chi_{yy})^2}. \quad (\text{B8})$$

Since $\chi_{xx} \neq \chi_{yy} \neq \chi_{xy} \neq \chi_{yx} \neq 0$ for the C_1 -symmetric meta-atom without mirror symmetry, the electric polarizability tensor $\hat{T}_{C_1}^f$ can be expressed as

$$\hat{T}_{C_1}^f = \hat{T}_{lin}^f = \begin{bmatrix} \chi_{xx} & \chi_{xy} \\ \chi_{xy} & \chi_{yy} \end{bmatrix}. \quad (\text{B9})$$

Therefore, the CPR of the C_1 -symmetric chiral meta-atom can be described as

the z axis. Therefore, the electric polarizability tensor of the C_n -symmetric chiral meta-atom satisfies the following relation:

$$D_{\frac{2\pi}{n}}^{-1} \hat{T}_{C_n}^f D_{\frac{2\pi}{n}} = \hat{T}_{C_n}^f. \quad (\text{B14})$$

By combining Eqs. (B2), (B4), and (B14), it can be derived that $\chi_{xy} = -\chi_{yx}$ and $\chi_{xx} = \chi_{yy}$ when $n > 2$. Therefore, for the C_n -symmetric chiral meta-atom, the electric polarizability tensor $\hat{T}_{C_n}^f$ can be expressed as

$$\hat{T}_{C_n}^f = \begin{bmatrix} \chi_{xx} & \chi_{xy} \\ -\chi_{xy} & \chi_{xx} \end{bmatrix}. \quad (\text{B15})$$

From Eqs. (B1) and (B15), the CPR of the C_n -symmetric chiral meta-atom can be described as

$$\text{CPR}_{C_n} = \frac{A_2^2}{A_1^2 + A_2^2} = \frac{0}{(2\chi_{xx})^2 + 0} = 0. \quad (\text{B16})$$

Actually, the conclusion of this paper, which is derived based on the dipole approximation, states that the CPR of C_n -symmetric ($n > 2$) meta-atoms is precisely 0 for the dipole radiation component. However, it is important to note that the CPR may not be exactly 0 for higher order multipole radiation components. Nevertheless, since the dipole is the dominant multipole component in antenna radiation, the CPR of the dipole component effectively reflects the CPR of the entire meta-atom to a considerable extent.

According to Eqs. (B8), (B10), (B13), and (B16), when $\chi_{xx} \neq \chi_{yy} \neq \chi_{xy} \neq \chi_{yx} \neq 0$, the order of the CPR

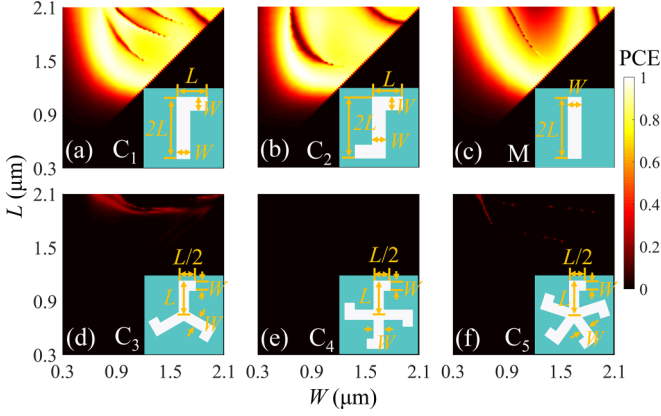


FIG. 6. PCE map as a function of the geometric parameters L and W ($L > W$) for different symmetric meta-atoms at a wavelength of $10.6 \mu\text{m}$. Inset: Schematic diagram illustrates meta-atoms with various symmetries, having a height $H = 6.8 \mu\text{m}$ and a period $P = 4.6 \mu\text{m}$.

for meta-atoms with different symmetries is as follows:

$$\text{CPR}_{C_1}, \text{CPR}_{C_2} > \text{CPR}_M > \text{CPR}_{C_n} (n > 2). \quad (\text{B17})$$

It should be noted that Eq. (B17) is valid under the assumption of the same polarizability tensor for each symmetric meta-atom, which can be challenging to satisfy in practice. In other words, Eq. (B17) implies that the parameter space for achieving high CPR in chiral C_1 - and C_2 -symmetric meta-atoms is larger compared to their corresponding mirror symmetric and other higher symmetric meta-atoms. To support this concept, Figs. 1, 6, and 7 illustrate the CPR, PCE and transmittance of different symmetric meta-atoms, respectively. The parameters are simplified to L and W ($L > W$) for a more intuitive comparison. The size of the high CPR region for different symmetric meta-atoms confirms the conclusion of Eq. (B17). In order to obtain the highest CPR and reduce the optimization parameters, the design of H-like shaped meta-atoms in this paper should satisfy chiral C_2 symmetry.

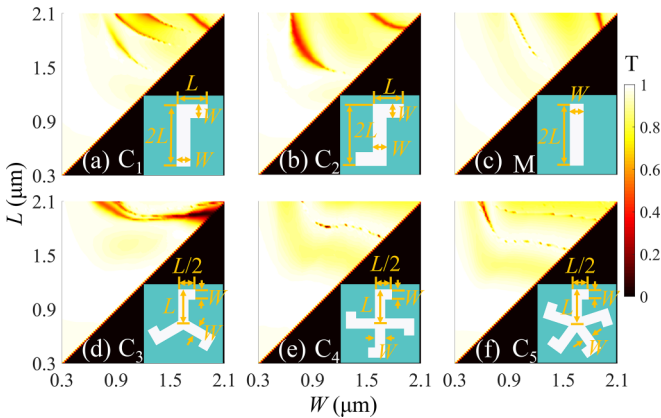


FIG. 7. Transmittance map as a function of the geometric parameters L and W ($L > W$) for different symmetric meta-atoms at a wavelength of $10.6 \mu\text{m}$. Inset: Schematic diagram illustrates meta-atoms with various symmetries, having $H = 6.8 \mu\text{m}$ and $P = 4.6 \mu\text{m}$.

APPENDIX C: DERIVATION OF ELECTRIC FIELD RESPONSE OF CHIRAL C_2 -SYMMETRIC META-ATOMS

According to Eq. (B12), for chiral C_2 -symmetric meta-atoms, Eq. (A7) can be simplified as

$$\begin{aligned} A_1 &= \frac{\varepsilon_0}{2} \sqrt{(\chi_{xx} + \chi_{yy})^2} \\ A_2 &= \frac{\varepsilon_0}{2} \sqrt{(\chi_{xx} - \chi_{yy})^2 + (2\chi_{xy})^2} \\ \varphi_1 &= 0 \\ \varphi_2 &= -\arctan \frac{2\chi_{xy}}{\chi_{xx} - \chi_{yy}}. \end{aligned} \quad (\text{C1})$$

Therefore, from Eqs. (A9) and (C1), the transmission electric field \vec{E}_t^f of the chiral C_2 -symmetric meta-atoms under forward illumination along the z direction can be expressed as

$$\vec{E}_t^f = \begin{cases} A_0(p_{LL}\vec{s}_L + p_{RL}\vec{s}_R) \\ = A_0(A_1\vec{s}_L + A_2e^{-j\varphi_2}\vec{s}_R), I_L \\ A_0(p_{LR}\vec{s}_L + p_{RR}\vec{s}_R) \\ = A_0(A_2e^{j\varphi_2}\vec{s}_L + A_1\vec{s}_R), I_R \end{cases}. \quad (\text{C2})$$

By applying the x -mirror symmetry operation \hat{M}_x to the C_2 -symmetric chiral meta-atoms, and considering Eqs. (B5) and (B12), the electric polarizability tensor $\hat{T}_{C_2\hat{M}_x}^f$ can be expressed as

$$\hat{T}_{C_2\hat{M}_x}^f = M_x^{-1} \hat{T}_{C_2}^f M_x = \begin{bmatrix} \chi_{xx} & -\chi_{xy} \\ -\chi_{xy} & \chi_{yy} \end{bmatrix}. \quad (\text{C3})$$

Substituting Eq. (C3) into Eq. (C1) gives

$$\begin{aligned} A_{1\hat{M}_x} &= \frac{\varepsilon_0}{2} \sqrt{(\chi_{xx} + \chi_{yy})^2} = A_1 \\ A_{2\hat{M}_x} &= \frac{\varepsilon_0}{2} \sqrt{(\chi_{xx} - \chi_{yy})^2 + (2\chi_{xy})^2} = A_2 \\ \varphi_{1\hat{M}_x} &= 0 = -\varphi_1 \\ \varphi_{2\hat{M}_x} &= \arctan \frac{2\chi_{xy}}{\chi_{xx} - \chi_{yy}} = -\varphi_2. \end{aligned} \quad (\text{C4})$$

Therefore, the expression for the transmission electric field $\vec{E}_{t\hat{M}_x}^f$ of the chiral C_2 -symmetric meta-atoms after the x -mirror symmetry operation \hat{M}_x , under forward illumination along the z direction, can be given as

$$\vec{E}_{t\hat{M}_x}^f = \begin{cases} A_0(A_1\vec{s}_L + A_2e^{j\varphi_2}\vec{s}_R), I_L \\ A_0(A_2e^{-j\varphi_2}\vec{s}_L + A_1\vec{s}_R), I_R \end{cases}. \quad (\text{C5})$$

Comparing Eqs. (C2) and (C5), it can be observed that the phase response of the C_2 -symmetric structure after the x -mirror symmetry operation \hat{M}_x is opposite to that before the mirror symmetry operation. In other words, if the phase delay before the mirror symmetry operation is $\varphi_{RL} = \varphi_a$ and $\varphi_{LR} = \varphi_b$, then the phase delay after the mirror symmetry operation is $\varphi_{RL} = \varphi_b$ and $\varphi_{LR} = \varphi_a$. Utilizing this property, we can compare the structures before and after the mirror symmetry operation to identify the structure that is closer to the target phase.

APPENDIX D: NUMERICAL SIMULATIONS

The numerical simulations in this paper utilize the finite-difference time-domain (FDTD) method implemented in the FDTD Solutions software developed by Lumerical, Canada. A mesh size of 130 nm is chosen to ensure the convergence of the results. The meta-atoms investigated in this study are composed of amorphous Si nano-antennas ($n_{\text{Si}} = 3.7400$) [36] placed on a BaF_2 substrate ($n_{\text{BaF}_2} = 1.4069$) [37]. These meta-atoms operate at a wavelength of $10.6 \mu\text{m}$, with a height of $H = 6.8 \mu\text{m}$ and a period of $P = 4.6 \mu\text{m}$.

The transmission phase, polarization conversion efficiency (PCE), and transmissivity of the unit cell were simulated by the FDTD method. Periodic boundary conditions were set along the x and y axes, and perfect matching layers were applied along the z axis to minimize reflection. A plane wave with circular polarization served as the incident light source. The PCE, which is defined as the ratio of the transmission with opposite chirality to the incidence, can also be expressed as the product of the CPR and transmissivity.

The focusing efficiency, focus length, full width half maximum (FWHM) of the metalens and far-field intensity profiles of the metalens were simulated by the FDTD method. Perfect matching layers were implemented along the x , y , and z directions. The light source used was a total-field scattered-field (TFSF) with circular or linear polarization. The focusing efficiency is defined as the ratio of the power at the focal spot to the incident power.

APPENDIX E: ADAPTIVE GENETIC ALGORITHM

The genetic algorithm [38,39] is a well-known global optimization technique renowned for its fast convergence and high accuracy. However, when applied to the optimization of H-like-shaped chiral C_2 -symmetric meta-atoms, which involve eight parameters and offer significant design flexibility, the simple genetic algorithm often becomes susceptible to local optima. To address this issue, we have adopted an adaptive genetic algorithm that incorporates self-adaptive mutation and crossover operations to optimize the H-like-shaped meta-atoms. To assess whether the optimization process becomes trapped in local optima, we have introduced a population entropy-based criterion. When the optimization process is identified to be trapped in a local optimum, the adaptive genetic algorithm executes a jump-out operation, enabling escape from the suboptimal solution and facilitating the attainment of global optimization. The flow diagram of the self-adaptive genetic algorithm is presented in Fig. 8.

Further details of these operations are described as follows.

Initialize population: The initial population comprised 30 randomly generated individuals, with their parameters encoded using the Gray coding technique.

Update population: The individuals in the population were evaluated to determine if they satisfied the constraint conditions. If any individual did not meet the conditions, it was regenerated until all individuals satisfied the constraints. The constraint conditions,

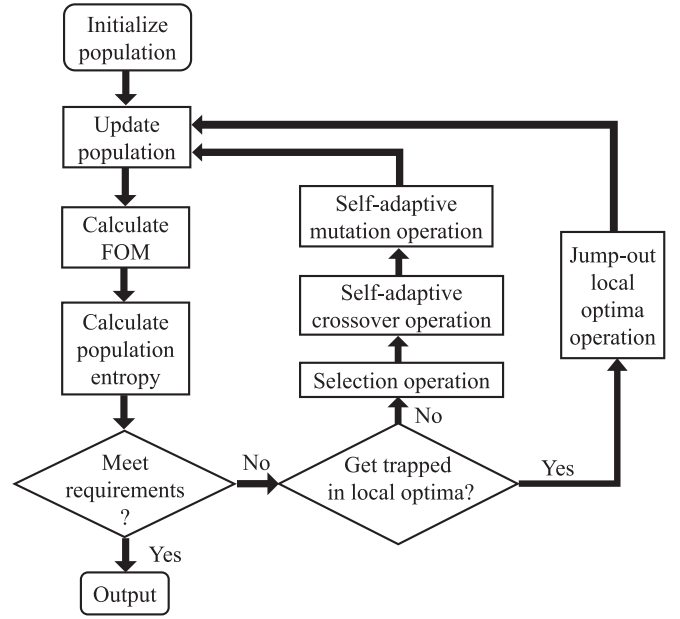


FIG. 8. Flow diagram of the self-adaptive genetic algorithm.

aimed at ensuring the manufacturability of the optimized meta-atoms and preventing overlap when rotating, included the conditions $(w_1 + w_2 + d_1 + d_2) < (P - 0.8 \mu\text{m})$, $[2\max(l_1, l_2) + w_3] < (P - 0.8 \mu\text{m})$, $[\min(d_1, d_2) + l_3/2] > (P/2)$, $[(P/2 - d_1)^2 + (w_3/2 + l_1)^2] < (P/2 - 0.4 \mu\text{m})^2$, and $[(P/2 - d_2)^2 + (w_3/2 + l_2)^2] < (P/2 - 0.4 \mu\text{m})^2$.

Calculate figure of merit (FOM): As mentioned in Sec. III and Appendix F, additional phase delays are caused by the offset of the PB phase and the change in the guide mode propagation phase. To minimize these additional phase delays, the actual phase response of the meta-atoms when rotated at 45° is taken into account in the FOM. The FOM for a single wavelength is defined as

$$\begin{aligned} \text{FOM}_0 &= \left| e^{|\Phi - \Phi_0|} + \frac{|T - T_0|}{T_0} \right| - 1 \\ \text{FOM}_{45} &= \left| e^{|\Phi_{45} - \Phi_0 + \frac{\pi}{2}\sigma|} + \frac{|T_{45} - T_0|}{T_0} \right| - 1 \\ \text{FOM} &= \frac{1}{0.3(\text{FOM}_0)^2 + 0.3(\text{FOM}_{45})^{1.5} - 0.6}, \end{aligned} \quad (\text{E1})$$

where Φ and Φ_0 are the actual and target phase, respectively, when the meta-atoms are rotated at 0° . Φ_{45} is the actual phase when the meta-atoms are rotated at 45° , and σ takes a value of -1 or $+1$ for RCP or LCP illumination. T and $T_0 = 1$ are the actual and target PCE when the meta-atoms are rotated at 0° , respectively. $T_{45} = 1$ is the target PCE when the meta-atoms are rotated at 45° . Therefore, the selection probability of each individual can be determined by

$$P_i = \frac{\text{FOM}_i}{\sum_{i=1}^N \text{FOM}_i}, \quad (\text{E2})$$

where P_i denotes the selection probability and FOM_i represents the FOM for the i th individual. $N = 30$ corresponds to the total number of individuals in the population.

Calculate population entropy: Similar to information entropy, population entropy can be used to quantify the degree of population diversity. The population entropy H_{pe} is defined as

$$H_{pe} = - \sum_{i=1}^N P_i \ln(P_i). \quad (\text{E3})$$

A higher population entropy indicates a lower degree of population diversity. The maximum population entropy is given by $H_{pe}^{\max} = \ln(N)$. If the $H_{pe} > 0.95H_{pe}^{\max}$ for two consecutive iterations, it can be inferred that the optimization process is trapped in a local optimum, necessitating the implementation of a jump-out operation to escape the suboptimal solution.

Selection operation: After calculating the selection probability for each individual, the Roulette Wheel method is employed to select the individual with high FOM for next iteration, with a selection rate of 0.5. However, when certain individuals exhibit significantly higher FOM compared to others, these super-individuals have a greater probability of being selected, increasing the risk of getting trapped in a local optimum due to reduced population diversity. To mitigate this, a FOM scale transformation is introduced for each individual prior to the selection process, which reduces the selection probability of super-individuals and increases the selection probability for individuals with lower FOM. Specifically, the transformed FOM, denoted as FOM' , for the i th individual is calculated as follows:

$$FOM' = \begin{cases} \text{ave}(FOM) + \mu \sqrt{\frac{FOM_i - \text{ave}(FOM)}{\mu}}, & [FOM_i \geq \text{ave}(FOM)] \\ \text{ave}(FOM) - \mu \sqrt{\frac{\text{ave}(FOM) - FOM_i}{\mu}}, & [FOM_i < \text{ave}(FOM)] \end{cases}, \quad (\text{E4})$$

where $\text{ave}(FOM)$ represents the average FOM in the population, and μ is defined as

$$\begin{aligned} \mu &= 0.5 \min(\mu_1, \mu_2) \\ \mu_1 &= \max(FOM) - \text{ave}(FOM) \\ \mu_2 &= \text{ave}(FOM) - \min(FOM), \end{aligned} \quad (\text{E5})$$

where $\max(FOM)$ and $\min(FOM)$ are the maximum and minimum FOM in the population, respectively.

Self-adaptive crossover operation: In genetic algorithms, the crossover probability p_c plays a crucial role in generating new individuals. A higher p_c accelerates the generation of new individuals but also poses a greater risk of destroying high FOM individuals. Conversely, a smaller p_c leads to a slower search speed. Hence, it is important to strike a balance between the evolutionary direction and search speed by appropriately adjusting the crossover probability. To address this, we employ a self-adaptive crossover operation that assigns a low crossover probability to individuals with high FOM and a high crossover probability to those with low FOM. The self-adaptive crossover probability p_c is defined as

$$p_c = \begin{cases} p_{c1} - \frac{(p_{c1} - p_{c2})(FOM_j - \text{ave}(FOM))}{\max(FOM) - \text{ave}(FOM)}, & [FOM_j \geq \text{ave}(FOM)] \\ p_{c1}, & [FOM_j < \text{ave}(FOM)] \end{cases}, \quad (\text{E6})$$

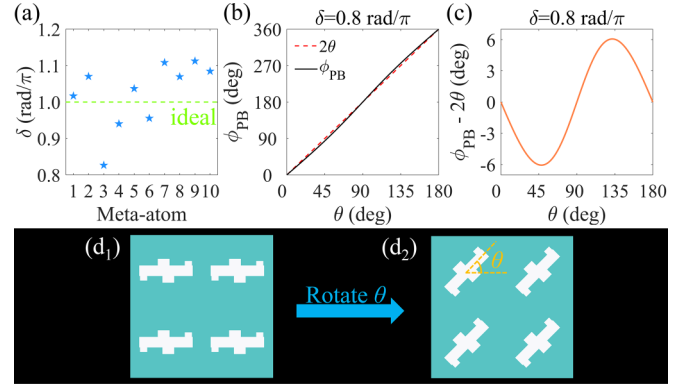


FIG. 9. (a) Retardations of 10 H-like shaped meta-atoms are marked by blue pentagrams, and the ideal retardation at $\delta = \pi$ is indicated by the green dash line. (b) Relationship between the actual ϕ_{PB} at a retardation of $\delta = 0.8 \text{ rad}/\pi$ (the ideal PB phase $\phi_{PB} = 2\theta$ at retardation of $\delta = 1 \text{ rad}/\pi$) and rotation angle θ . (c) Discrepancy between the actual and ideal PB phase for various rotation angles. (d) Schematic diagram of the arrangement alteration upon the rotation of the meta-atoms.

where FOM_j represents the higher FOM value between the two parents selected for the crossover operation. The $p_{c1} = 0.9$ and $p_{c2} = 0.3$. We applied the multipoint crossover operation, with the ratio of crossover points to the overall number of points in the individuals p_{cn} is set as $p_{cn} = p_c^3$.

Self-adaptive mutation operation: Increasing the mutation probability p_m , akin to the crossover probability p_c , expedites the generation of new individuals while simultaneously amplifying the attrition of high FOM individuals. Conversely, reducing the value of p_m diminishes the search speed. Consequently, to mitigate these concerns, we implement a self-adaptive mutation operation, wherein individuals with high FOM are allocated a low mutation probability and those with low FOM are assigned a high mutation probability. The expression denoting the self-adaptive mutation probability,

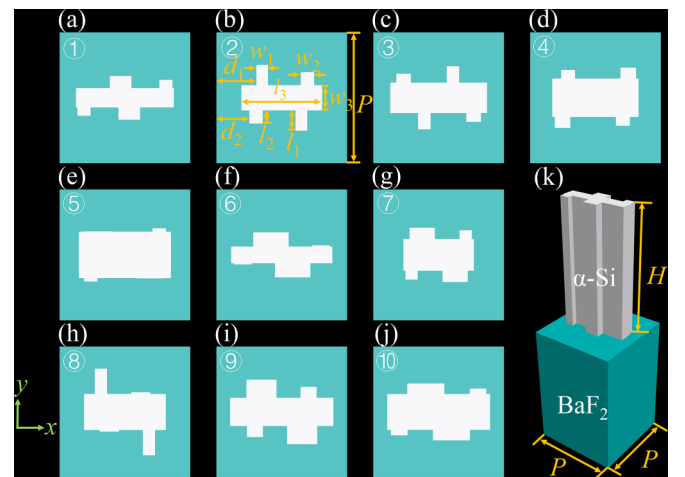


FIG. 10. (a)–(j) Top view of 10 optimized H-like-shaped meta-atoms. (k) Side view of the optimized meta-atom 1. The geometric parameters are marked in yellow in (b) and (k). $H = 6.8 \mu\text{m}$, $P = 4.6 \mu\text{m}$.

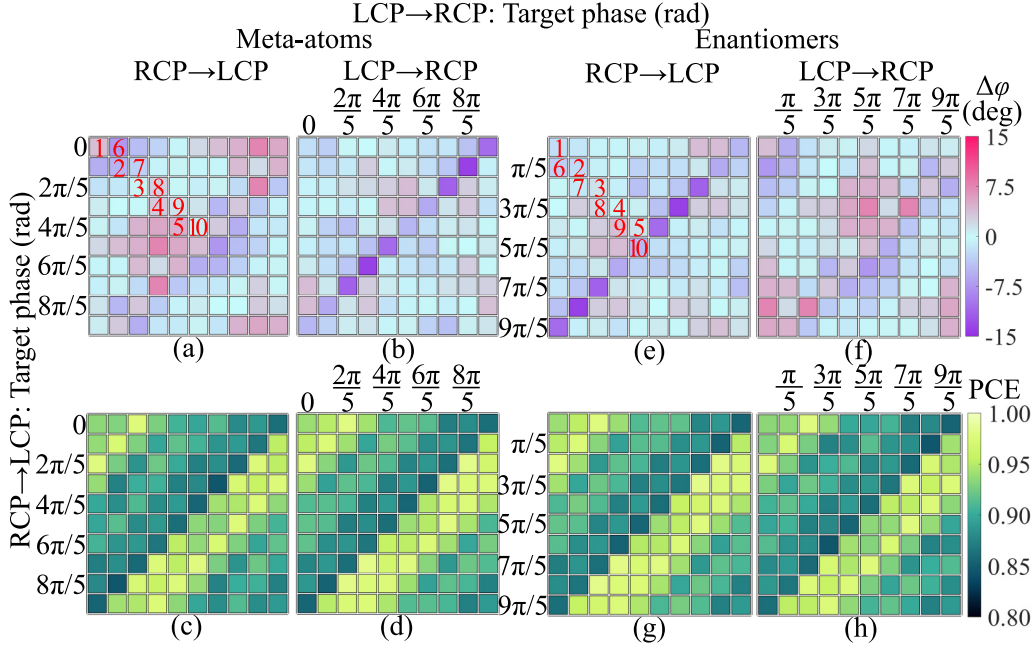


FIG. 11. Phase libraries for spin-decoupled modulation. (a)–(d), the phase library comprises combinations of meta-atoms with their PB phase delay. (e)–(h), enantiomers are combined with their PB phase delay. (a), (b), (e), (f) are phase differences ($\Delta\phi$) between reality and target. The red number indicates the corresponding meta-atoms (a) and enantiomers (e) without rotation. (c), (d), (g), (h) are maps of the polarization conversion efficiency (PCE).

p_m , is given as follows:

$$p_m = \begin{cases} p_{m1} - \frac{(p_{m1} - p_{m2})(\max(\text{FOM}) - \text{FOM}_k)}{\max(\text{FOM}) - \text{ave}(\text{FOM})}, & [\text{FOM}_k \geq \text{ave}(\text{FOM})] \\ p_{m1}, & [\text{FOM}_k < \text{ave}(\text{FOM})] \end{cases}, \quad (\text{E7})$$

where FOM_k is the FOM of the individual prepared for the mutation operation. The $p_{m1} = 0.2$ and $p_{m2} = 0.01$. The ratio of mutation points to the total number of points in the individuals p_{mn} is set as $p_{mn} = p_m^2$.

Jump-out local optima operation: As previously mentioned, we consider the optimization process to be trapped in local optima if the $H_{pe} > 0.95H_{pe}^{\max}$ for two consecutive iterations. To address this situation, we employ the jump-out local optima operation, which involves modifying the selection, crossover, and mutation operations. For the selection operation, the selection rate is reduced to 0.1. In the crossover operation, the crossover probability p_c is increased to 0.9, and the crossover point ratio p_{cn} is set to 0.5. Regarding the mutation operation, in addition to changing the mutation probability p_{cm} to 0.9, we adopt the bitwise mutation operation. In a population with binary coding, the monotonic coefficient of the i th coded bit can be defined as

$$\mu_i = \left| \frac{1}{N} \sum_{j=1}^N x_{ji} - 0.5 \right| \times 2, \quad (j = 1, 2, \dots, N; \quad i = 1, 2, \dots, M), \quad (\text{E8})$$

where the μ_i is the monotonic coefficient of the i th coded bit. x_{ij} signifies the i th coded bit value of the j th individual in the population. N denotes the total number of individuals in the population, and M represents the total number of coding bits

of the individual. When all the numbers in the i th bit of the population are exclusively 0 or 1, $\mu_i = 1$. Conversely, if the i th bit of the population consists of an equal number of zeros and ones, $\mu_i = 0$. During the bitwise mutation operation, the mutation probability for the i th coding position of the j th individual is determined as $p_{mji} = \mu_i/2$.

Optimization termination: If the maximum FOM remains unchanged after five continuous jump-out local optima operations, it can be considered as the global optimum solution. Otherwise the algorithm will terminate at the 200th generations.

APPENDIX F: ANALYSIS OF PHASE DELAY OFFSET

Figure 9(a) displays the real retardation δ of 10 kinds of H-like-shaped meta-atoms, which deviate from the ideal retardation ($\delta = \pi$), resulting in a phase delay offset in comparison to the ideal PB phase delay. In Figs. 9(b) and 9(c), a phase delay offset of up to 6° is observed when the real retardation is equal to 0.8π at a rotated angle of 45° .

Furthermore, while the phase delay of guided mode propagation is independent of the rotation angle, the arrangement within the array does impact the phase delay and PCE. Figure 9(d) illustrates that when the meta-atom is rotated by an angle θ , the arrangement is modified, resulting in a change in the phase response of guided mode propagation.

APPENDIX G: ANALYSIS OF ASYMMETRY FOCUS SPOT WITH LINEAR POLARIZATION INCIDENT

For linearly polarized light incident at a polarization angle γ with respect to the x axis, the excited dipole moment in the

anisotropic crystal can be expressed as

$$\begin{aligned} \begin{bmatrix} p_x \\ p_y \end{bmatrix} &= \begin{bmatrix} P_x \\ P_y \end{bmatrix} = \varepsilon_0 \begin{bmatrix} \chi_{xx} & \chi_{xy} \\ \chi_{yx} & \chi_{yy} \end{bmatrix} \begin{bmatrix} E_{xi} \\ E_{yi} \end{bmatrix} \\ &= \varepsilon_0 \begin{bmatrix} \chi_{xx} & \chi_{xy} \\ \chi_{yx} & \chi_{yy} \end{bmatrix} \begin{bmatrix} \cos \gamma \\ \sin \gamma \end{bmatrix}, \end{aligned} \quad (\text{G1})$$

where $\vec{p} = p_x \vec{e}_x + p_y \vec{e}_y$. The transmitted electric field \vec{E}'_t can be expressed as

$$\begin{aligned} \vec{E}'_t &= A_0 \left[p_x \vec{e}_x + p_y \vec{e}_y - \frac{1}{\sqrt{2}} \sin \xi (p_x + p_y) \vec{e}_{R_0} \right] \\ &= A_0 \varepsilon_0 \left[(\chi_{xx} \cos \gamma + \chi_{xy} \sin \gamma) \vec{e}_x \right. \\ &\quad + (\chi_{yx} \cos \gamma + \chi_{yy} \sin \gamma) \vec{e}_y \\ &\quad - \frac{1}{\sqrt{2}} \sin \xi (\chi_{xx} \cos \gamma + \chi_{xy} \sin \gamma \\ &\quad \left. + \chi_{yx} \cos \gamma + \chi_{yy} \sin \gamma) \vec{e}_{R_0} \right]. \end{aligned} \quad (\text{G2})$$

This equation indicates that the excited dipole moment in the anisotropic crystal is dependent on the incident polarization direction γ . Consequently, the radiation pattern is influenced by the incident polarization direction γ . A larger angle ξ between the observation direction \vec{e}_{R_0} and z axis (corresponding to a larger $\sin \xi$) implies a more nonuniform radiation pattern. In summary, when linearly polarized light is incident, a larger NA of the metalens leads to larger dipolar radiation angles at the metalens edge, resulting in a more nonuniform focal point pattern.

APPENDIX H: DETAILS OF META-ATOMS AND PHASE LIBRARY

Figure 10 illustrates the schematic of ten optimized H-like-shaped meta-atoms. Figure 11 displays the phase difference between reality and target in the unoptimized phase library and the PCE of the library. Figure 2 shows the optimized library, achieved through a meticulous comparison of $\Delta\varphi$ between the meta-atoms and their enantiomers. Comparing the unoptimized library composed solely of meta-atoms [Figs. 11(a), 11(b)] and enantiomers [Figs. 11(e), 11(f)] with the optimized library [Figs. 2(c), 2(d)], the phase difference in the optimized library is smaller than that in the unoptimized counterparts.

-
- [1] C. W. Qiu, T. Zhang, G. Hu, and Y. Kivshar, Quo vadis, meta-surfaces? *Nano Lett.* **21**, 5461 (2021).
- [2] N. Yu, P. Genevet, M. A. Kats, F. Aieta, J. P. Tetienne, F. Capasso, and Z. Gaburro, Light propagation with phase discontinuities: Generalized laws of reflection and refraction, *Science* **334**, 333 (2011).
- [3] S. Sun, Q. He, S. Xiao, Q. Xu, X. Li, and L. Zhou, Gradient-index meta-surfaces as a bridge linking propagating waves and surface waves, *Nat. Mater.* **11**, 426 (2012).
- [4] W. T. Chen, A. Y. Zhu, and F. Capasso, Flat optics with dispersion-engineered metasurfaces, *Nat. Rev. Mater.* **5**, 604 (2020).
- [5] M. Pan, Y. Fu, M. Zheng, H. Chen, Y. Zang, H. Duan, Q. Li, M. Qiu, and Y. Hu, Dielectric metalens for miniaturized imaging systems: Progress and challenges, *Light Sci. Appl.* **11**, 195 (2022).
- [6] C. Chen, S. Gao, W. Song, H. Li, S. N. Zhu, and T. Li, Metasurfaces with planar chiral meta-atoms for spin light manipulation, *Nano Lett.* **21**, 1815 (2021).
- [7] J. P. Balthasar Mueller, N. A. Rubin, R. C. Devlin, B. Groever, and F. Capasso, Metasurface polarization optics: Independent phase control of arbitrary orthogonal states of polarization, *Phys. Rev. Lett.* **118**, 113901 (2017).
- [8] J. Jin, J. Luo, X. Zhang, H. Gao, X. Li, M. Pu, P. Gao, Z. Zhao, and X. Luo, Generation and detection of orbital angular momentum via metasurface, *Sci. Rep.* **6**, 24286 (2016).
- [9] X. Zhang, L. Huang, R. Zhao, Q. Wei, X. Li, G. Geng, J. Li, X. Li, Y. Wang, and S. Zhang, Multiplexed generation of generalized vortex beams with on-demand intensity profiles based on metasurfaces, *Laser Photonics Rev.* **16**, 2100451 (2022).
- [10] J. Li, P. Yu, S. Zhang, and N. Liu, Electrically-controlled digital metasurface device for light projection displays, *Nat. Commun.* **11**, 3574 (2020).
- [11] M. Y. Shalaginov, S. An, Y. Zhang, F. Yang, P. Su, V. Liberman, J. B. Chou, C. M. Roberts, M. Kang, C. Rios *et al.*, Reconfigurable all-dielectric metalens with diffraction-limited performance, *Nat. Commun.* **12**, 1225 (2021).
- [12] F. Zhang, X. Xie, M. Pu, Y. Guo, X. Ma, X. Li, J. Luo, Q. He, H. Yu, and X. Luo, Multistate switching of photonic angular momentum coupling in phase-change metadevices, *Adv. Mater.* **32**, 1908194 (2020).
- [13] I. Kim, M. A. Ansari, M. Q. Mehmood, W. S. Kim, J. Jang, M. Zubair, Y. K. Kim, and J. Rho, Stimuli-responsive dynamic metaholographic displays with designer liquid crystal modulators, *Adv. Mater.* **32**, 2004664 (2020).
- [14] M. K. Park, C. S. Park, Y. S. Hwang, E. S. Kim, D. Y. Choi, and S. S. Lee, Virtual-moving metalens array enabling light-field imaging with enhanced resolution, *Adv. Opt. Mater.* **8**, 2000820 (2020).
- [15] Z. Shi, A. Y. Zhu, Z. Li, Y. W. Huang, W. T. Chen, C. W. Qiu, and F. Capasso, Continuous angle-tunable birefringence with freeform metasurfaces for arbitrary polarization conversion, *Sci. Adv.* **6**, eaba3367 (2020).
- [16] Y. Zhou, I. I. Kravchenko, H. Wang, H. Zheng, G. Gu, and J. Valentine, Multifunctional metaoptics based on bilayer metasurfaces, *Light Sci. Appl.* **8**, 80 (2019).
- [17] X. Fang, H. Ren, and M. Gu, Orbital angular momentum holography for high-security encryption, *Nat. Photonics* **14**, 102 (2020).
- [18] S. S. Kruk, L. Wang, B. Sain, Z. Dong, J. Yang, T. Zentgraf, and Y. Kivshar, Asymmetric parametric generation of images

- with nonlinear dielectric metasurfaces, *Nat. Photonics* **16**, 561 (2022).
- [19] C. Chen, X. Ye, J. Sun, Y. Chen, C. Huang, X. Xiao, W. Song, S. Zhu, and T. Li, Bifacial-metasurface-enabled pancake metalens with polarized space folding, *Optica* **9**, 1314 (2022).
- [20] F. Zhang, Y. Guo, M. Pu, L. Chen, M. Xu, M. Liao, L. Li, X. Li, X. Ma, and X. Luo, Meta-optics empowered vector visual cryptography for high security and rapid decryption, *Nat. Commun.* **14**, 1946 (2023).
- [21] Y. Chen, X. Yang, and J. Gao, Spin-controlled wavefront shaping with plasmonic chiral geometric metasurfaces, *Light Sci. Appl.* **7**, 84 (2018).
- [22] X. Zhang, S. Yang, W. Yue, Q. Xu, C. Tian, X. Zhang, E. Plum, S. Zhang, J. Han, and W. Zhang, Direct polarization measurement using a multiplexed Pancharatnam-Berry metahologram, *Optica* **6**, 1190 (2019).
- [23] R. Jin, L. Deng, L. Tang, Y. Cao, Y. Liu, and Z. G. Dong, Decoupled phase modulation for circularly polarized light via chiral metasurfaces, *ACS Photonics* **10**, 155 (2023).
- [24] G. D. Bai, Q. Ma, R. Q. Li, J. Mu, H. B. Jing, L. Zhang, and T. J. Cui, Spin-symmetry breaking through metasurface geometric phases, *Phys. Rev. Appl.* **12**, 044042 (2019).
- [25] Y. Yuan, K. Zhang, B. Ratni, Q. Song, X. Ding, Q. Wu, S. N. Burokur, and P. Genevet, Independent phase modulation for quadruplex polarization channels enabled by chirality-assisted geometric-phase metasurfaces, *Nat. Commun.* **11**, 4186 (2020).
- [26] Y. Guo, M. Pu, Z. Zhao, Y. Wang, J. Jin, P. Gao, X. Li, X. Ma, and X. Luo, Merging geometric phase and plasmon retardation phase in continuously shaped metasurfaces for arbitrary orbital angular momentum generation, *ACS Photonics* **3**, 2022 (2016).
- [27] T. Li, C. Chen, X. Xiao, J. Chen, S. Hu, and S. Zhu, Revolutionary meta-imaging: From superlens to metalens, *Photon. Insights* **2**, R01 (2023).
- [28] J. Kim, A. S. Rana, Y. Kim, I. Kim, T. Badloe, M. Zubair, M. Q. Mehmood, and J. Rho, Chiroptical metasurfaces: Principles, classification, and applications, *Sensors* **21**, 4381 (2021).
- [29] C. Menzel, C. Rockstuhl, and F. Lederer, Advanced jones calculus for the classification of periodic metamaterials, *Phys. Rev. A* **82**, 053811 (2010).
- [30] X. Xie, M. Pu, J. Jin, M. Xu, Y. Guo, X. Li, P. Gao, X. Ma, and X. Luo, Generalized Pancharatnam-Berry phase in rotationally symmetric meta-atoms, *Phys. Rev. Lett.* **126**, 183902 (2021).
- [31] G. Li, S. Zhang, and T. Zentgraf, Nonlinear photonic metasurfaces, *Nat. Rev. Mater.* **2**, 17010 (2017).
- [32] Y. T. Lim, J. H. Park, K. C. Kwon, and N. Kim, Resolution-enhanced integral imaging microscopy that uses lens array shifting, *Opt. Express* **17**, 19253 (2009).
- [33] C. P. Jisha, S. Nolte, and A. Alberucci, Geometric phase in optics: From wavefront manipulation to waveguiding, *Laser Photonics Rev.* **15**, 2100003 (2021).
- [34] M. Liu, Q. Fan, L. Yu, and T. Xu, Polarization-independent infrared micro-lens array based on all-silicon metasurfaces, *Opt. Express* **27**, 10738 (2019).
- [35] M. Dong, C. Zhang, M. Ren, R. Albarracin, and R. Ye, Electrochemical and infrared absorption spectroscopy detection of SF₆ decomposition products, *Sensors* **17**, 2627 (2017).
- [36] H. Piller, Silicon (amorphous) (a-Si), in *Handbook of Optical Constants of Solids*, edited by E. D. Palik (Academic Press, Burlington, 1997), pp. 571–586.
- [37] M. R. Querry, Optical constants of minerals and other materials from the millimeter to the ultraviolet, Contractor Report CRDEC-CR-88009 (1987), <https://apps.dtic.mil/sti/citations/ADA192210>.
- [38] S. Xiao, F. Zhao, D. Wang, J. Weng, Y. Wang, X. He, H. Chen, Z. Zhang, Y. Yu, Z. Zhang, Z. Zhang, and J. Yang, Inverse design of a near-infrared metalens with an extended depth of focus based on double-process genetic algorithm optimization, *Opt. Express* **31**, 8668 (2023).
- [39] H. Liang, Q. Lin, X. Xie, Q. Sun, Y. Wang, L. Zhou, L. Liu, X. Yu, J. Zhou, T. F. Krauss, and J. Li, Ultrahigh numerical aperture metalens at visible wavelengths, *Nano Lett.* **18**, 4460 (2018).
- [40] C. Pfeiffer and A. Grbic, Metamaterial Huygens' surfaces: Tailoring wave fronts with reflectionless sheets, *Phys. Rev. Lett.* **110**, 197401 (2013).
- [41] L. Li, Z. Liu, X. Ren, S. Wang, V. C. Su, M. K. Chen, C. H. Chu, H. Y. Kuo, B. Liu, W. Zang *et al.*, Metalens-array-based high-dimensional and multiphoton quantum source, *Science* **368**, 1487 (2020).
- [42] X. Shi, D. Meng, Z. Qin, Q. He, S. Sun, L. Zhou, D. R. Smith, Q. H. Liu, T. Bourouina, and Z. Liang, All-dielectric orthogonal doublet cylindrical metalens in long-wave infrared regions, *Opt. Express* **29**, 3524 (2021).
- [43] Y. Zhu, S. Zhou, Z. Wang, X. Pu, X. Cao, Y. Yu, W. Yuan, and W. Liu, High-efficiency all-silicon metasurfaces with 2π phase control based on multiple resonators, *Res. Phys.* **29**, 104765 (2021).
- [44] D. Shan, J. Gao, N. Xu, H. Liu, N. Song, Q. Sun, Y. Zhao, Y. Tang, Y. Wang, X. Feng, and X. Chen, Bandpass filter integrated metalens based on electromagnetically induced transparency, *Nanomaterials* **12**, 2282 (2022).
- [45] H. Hou, Y. Zhang, Z. Luo, P. Zhang, and Y. Zhao, Design and fabrication of monolithically integrated metalens for higher effective fill factor in long-wave infrared detectors, *Opt. Lasers Eng.* **150**, 106849 (2022).